The effect of swirl on jets and wakes: Linear instability of the Rankine vortex with axial flow

T. Loiseleux, J. M. Chomaz, and P. Huerre
Laboratoire d'Hydrodynamique, CNRS-UMR 156, Ecole Polytechnique F-91128 Palaiseau, France

(Received 23 July 1997; accepted 26 November 1997)

The effect of swirl on jets and wakes is investigated by analyzing the inviscid spatiotemporal instability of the Rankine vortex with superimposed plug flow axial velocity profile. The linear dispersion relation is derived analytically as a function of two nondimensional control parameters: the swirl ratio S and the external axial flow parameter a ($a>-0.5$ for jets, $a<-0.5$ for wakes). For each azimuthal wave number m, there exists a single unstable Kelvin–Helmholtz mode and an infinite number of neutrally stable inertial waveguide modes. Swirl decreases the temporal growth rate of the *axisymmetric* Kelvin–Helmholtz mode ($m=0$), which nonetheless remains unstable for all axial wave numbers. For *helical* modes ($m\neq 0$), small amounts of swirl lead to the widespread occurrence of direct resonances between the unstable Kelvin–Helmholtz mode and the inertial waveguide modes. Such interactions generate, in the low wave number range, neutrally stable wave number bands separated by bubbles of instability. As S increases above a critical value, all bubbles merge to give rise to unstable wave numbers throughout, but the growth rate envelope decreases continuously with increasing swirl. In the high wave number range, negative helical mode growth rates are enhanced for small swirl and decrease continuously for large swirl, while positive helical mode growth rates monotonically decrease with increasing swirl. For a given positive swirl, negative modes are more unstable than their positive counterparts, although their growth rates may not necessarily be larger than in the nonrotating case. The absolute/convective nature of the instability in swirling jets and wakes is determined in an $a-S$ control parameter plane by numerical implementation of the Briggs–Bers criterion. In the absence of swirl, *jets* ($a>-0.5$) become absolutely unstable (AI) to the axisymmetric mode $m=0$ only for a sufficiently large external axial counterflow $a<-0.15$. AI is found to be significantly enhanced by swirl: for $S>1.61$, AI occurs, even for coflowing jets ($a>0$). As S is gradually increased, the transitional mode to AI successively becomes $m=0, -1, -2, -3$, etc. In the absence of swirl, *wakes* ($a<-0.5$) become absolutely unstable to the bending modes $m=\pm 1$ only for sufficiently large counterflow $1+a>0.091$. For $S>0.47$, AI occurs even for coflowing wakes ($a<-1$) and, as S increases, the transitional mode to AI successively becomes $m=-1, -2, -3$, etc. This instability analysis is found to provide a preliminary estimate of the critical Rossby number for the onset of vortex breakdown: for zero external axial flow jets ($a=0$), absolute/convective transition first takes place at a Rossby number $\mathrm{Ro}\equiv S^{-1}\sim 0.62$, which very favorably compares with available experimental and numerical threshold values for vortex breakdown onset. © *1998 American Institute of Physics.*
[S1070-6631(98)02103-5]

I. INTRODUCTION

The evolution of coherent structures in jets and wakes is known to be very sensitive to the nature of the underlying basic flow field. For instance, density variations, counterflow or cross-flow velocities, surface tension effects and rotation may induce qualitative changes in the observed flow states, thereby leading to noise amplification, synchronized oscillations (Huerre and Monkewitz[1]), transition to turbulence (Lingwood[2]), etc. These features may also be used to advantage in order to effectively manipulate the flow dynamics. Linear instability theory provides the natural framework for a quantitative investigation of these phenomena.

The objective of the present study is to assess the effect of swirl on the unsteady development of axisymmetric jets and wakes. We choose to focus on one of the simplest basic flow models, namely the plug flow axial velocity profile investigated by Batchelor and Gill,[3] to which is superimposed a solid body core rotation in the form of a Rankine vortex (Thomson,[4] Moore and Saffman,[5] Saffman[6]). Such a velocity distribution is a first approximation to the measured axial and azimuthal velocity profiles prevailing close to the nozzle exit in free swirling jets, as studied experimentally by Panda and McLaughlin[7] and Billant, Chomaz and Huerre.[8] This configuration has recently been found to exhibit a variety of breakdown states[8] above a critical value of the swirl parameter.

Related earlier theoretical studies have considered the temporal (Lessen and Paillet,[9] Lessen, Singh and Paillet,[10] Khorrami[11]) and spatiotemporal (Olendraru, Sellier, Rossi, and Huerre,[12] and Delbende, Chomaz, and Huerre[13]) instability properties of the Batchelor q vortex, a flow that is a

more appropriate representation of the basic state in the fully developed region of swirling jets, in trailing line vortices, or in the concentrated vortices generated in confined tube experiments. In particular, the Batchelor q vortex has been shown to undergo a transition to absolute instability for sufficiently large swirl, even in the absence of axial counterflow.[12,13] The temporal instability characteristics of a self-similar fully developed swirling jet solution derived by Görtler[14] have recently been analyzed in detail as a function of swirl ratio, Mach number, and Reynolds number by Khorrami.[15]

The goal of the present study is to perform a corresponding instability analysis for the Rankine vortex with axial flow, and to ultimately relate absolute/convective (AI/CI) transition to the onset of vortex breakdown. The AI/CI transition of instability waves considered here in the context of swirling jets and wakes constitutes a natural generalization of two earlier theoretical approaches to the vortex breakdown problem: the supercritical/subcritical transition theory advocated by Benjamin[16] in the framework of neutrally stable nondispersive inertial waves and the group velocity criterion developed by Tsai and Widnall[17] for dispersive inertial waves. In all instances, vortex breakdown is characterized as a transition from a supercritical state supporting only downstream traveling waves to a subcritical state supporting both upstream and downstream traveling waves.

A distinct advantage of the Rankine vortex with axial flow stems from the fact that the dispersion relation can be obtained analytically in terms of transcendental functions. According to Batchelor and Gill,[3] the plug flow jet in the absence of swirl is unstable for all axial wave numbers to both axisymmetric and helical modes. By contrast, the studies of Thomson,[4] Moore and Saffman,[5] and Saffman[6] have established that the Rankine vortex in the absence of axial flow only exhibits a countable infinity of neutrally stable dispersive inertial waves for each axisymmetric or helical mode index. In the present study we intend to fill the gap between these two limiting cases by answering the following question: what is the effect of swirl on the Kelvin–Helmholtz instability of jets and wakes? Note that piecewise continuous basic velocity profiles such as the Caflisch cylindrical vortex sheet model with axial flow (Caflisch, Li and Shelley[18] and Martin and Meiburg[19]) or plane plug-flow jets and wakes with density jumps (Yu and Monkewitz[20]) have recently proved to be convenient analytical models both for purely temporal stability analyses and for the determination of AI/CI boundaries.

The paper is organized as follows: the linear dispersion relation pertaining to the Rankine vortex with axial flow is derived in Sec. II. In Sec. III, asymptotic expansions for the temporal instability properties are summarized both in the high and low wave number regimes (Sec. III A). These analytical approximations then serve as a convenient guide to interpret the numerical results presented in Sec. III B. The absolute/convective nature of the instability is investigated in Sec. IV by numerical implementation of the Briggs–Bers criterion (Sec. IV A). AI/CI transition in jets is discussed in Sec. IV B for axisymmetric modes and in Sec. IV C for helical modes. Corresponding results for wakes are presented in Sec. IV D. We summarize in Sec. V the extent of the AI domain in the control parameter plane defined by the swirl ratio S and the external axial flow parameter a. The study concludes with a discussion of the relationship between AI/CI transition and vortex breakdown onset, as obtained in various experiments and numerical simulations.

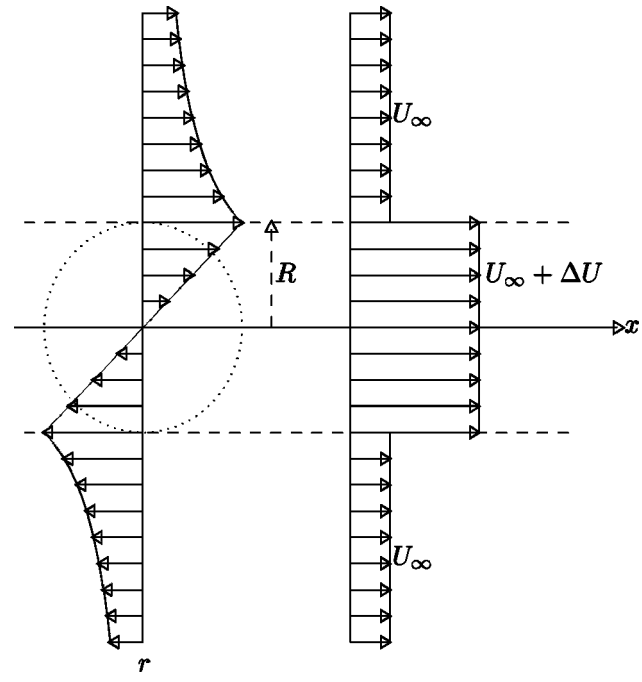

FIG. 1. Sketch of basic flow azimuthal and axial velocity profiles $W(r)$ and $U(r)$.

II. PROBLEM FORMULATION AND LINEAR DISPERSION RELATION

In the entire study, the flow is assumed to be inviscid, incompressible of density ρ and governed by the Euler equations. The basic flow under consideration consists of a Rankine vortex of core radius R aligned along the x axis, upon which is superimposed a plug flow axial velocity profile, as sketched in Fig. 1. Let U, V, W denote the axial, radial, and azimuthal velocity components in the usual x, r, θ cylindrical coordinate system of unit vectors $\mathbf{e_x}$, $\mathbf{e_r}$, $\mathbf{e_\theta}$. The basic velocity field is then given by

$$U(r)=U_\infty+\Delta U,\quad V(r)=0,\quad W(r)=\Omega r,\qquad \text{if } r<R, \tag{1a}$$

$$U(r)=U_\infty,\qquad V(r)=0,\quad W(r)=\Omega R^2/r,\quad \text{if } r>R, \tag{1b}$$

where U_∞ is the external axial velocity, ΔU the axial velocity difference across the vortex sheet $r=R$, and Ω the solid body rotation rate in the core. The basic vorticity $\boldsymbol{\omega}=\boldsymbol{\nabla}\times\mathbf{U}$ and pressure P then readily follow in the form

$$\boldsymbol{\omega}(r)=2\Omega\mathbf{e}_x,\quad P(r)=P_\infty-\rho\Omega^2(R^2-r^2/2),\quad \text{if } r<R, \tag{2a}$$

$$\boldsymbol{\omega}(r)=0,\qquad P(r)=P_\infty-\frac{1}{2}\rho\Omega^2R^4r^{-2},\qquad \text{if } r>R, \tag{2b}$$

where P_∞ is the external pressure at $r=\infty$.

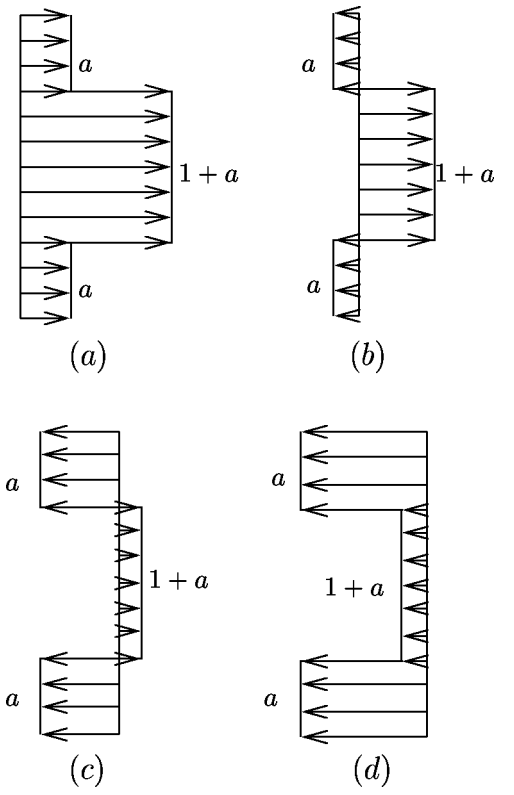

FIG. 2. Evolution of the axial velocity profile with external flow parameter a. (a) $a \geqslant 0$: jet with coflow. (b) $-0.5 \leqslant a \leqslant 0$: jet with counterflow. (c) $-1 \leqslant a \leqslant -0.5$: wake with counterflow. (d) $a \leqslant -1$: wake with coflow.

The basic flow is seen to effectively depend on two nondimensional control parameters: the external flow a and the swirl S, which are defined as

$$a \equiv \frac{U_\infty}{\Delta U}, \quad S \equiv \frac{\Omega R}{\Delta U}. \tag{3}$$

For further reference, note that the Rossby number Ro is then simply $\mathrm{Ro} = 1/S$. Distinct configurations are obtained by varying a within specific ranges, as illustrated in Fig. 2. The external and core streams are coflowing when $a < -1$ or $a > 0$ and counterflowing when $-1 < a < 0$. Jets correspond to $a > -0.5$ and wakes to $a < -0.5$. The particular values $a = 0$ and $a = -1$ are associated with the zero external flow jet and zero centerline velocity wake, respectively.

The linear dispersion relation is derived by first linearizing the Euler equations around the basic flow $U(r)$, $W(r)$ specified in (1a) and (1b). The perturbation velocity components u, v, w and pressure p are then decomposed into normal modes of the form

$$\{u,v,w,p\} = \{\hat{u}(r),\hat{v}(r),\hat{w}(r),\hat{p}(r)\}e^{i(kz+m\theta-\omega t)}, \tag{4}$$

where k is the complex axial wave number, m the integer azimuthal wave number, and ω the complex frequency. Two distinct systems of ordinary differential equations are then obtained for the eigenfunctions $\hat{u}(r)$, $\hat{v}(r)$, $\hat{w}(r)$, and $\hat{p}(r)$ in the regions $r < R$ and $r > R$. Corresponding solutions have to be related via appropriate jump conditions across the displaced interface. In the linearized approximation, such conditions can be transferred on the undisturbed vortex sheet at $r = R$. The procedure is outlined below.

In the core $r < R$, dimensional perturbations are found to satisfy

$$\hat{u}'(r) + r^{-1}\hat{u}(r) + imr^{-1}\hat{v}(r) + ik\hat{w}(r) = 0, \tag{5a}$$

$$i\omega_j\hat{u}(r) + 2\Omega\hat{v}(r) = \rho^{-1}\hat{p}'(r), \tag{5b}$$

$$i\omega_j\hat{v}(r) + 2\Omega\hat{u}(r) = (\rho r)^{-1}im\hat{p}(r), \tag{5c}$$

$$\omega_j\hat{w}(r) = \rho^{-1}k\hat{p}(r). \tag{5d}$$

In the above system,

$$\omega_j \equiv \omega - m\Omega - (U_\infty + \Delta U)k \tag{6}$$

denotes the Doppler shifted frequency in a frame of reference moving with the basic flow within the core. Via elementary manipulations of (5a)–(5d) it is straightforward to show that the pressure eigenfunction $\hat{p}(r)$ is governed by

$$r^2\hat{p}''(r) + r\hat{p}'(r) + [k^2r^2(4\Omega^2\omega_j^{-2} - 1) - m^2]\hat{p}(r) = 0. \tag{7}$$

The general solution of (7) is $\hat{p}(r) = A_1 J_m(\beta r) + B_1 Y_m(\beta r)$, where J_m and Y_m are the Bessel functions of first and second kind of order $|m|$, and β is defined by

$$\beta^2 \equiv k^2(4\Omega^2\omega_j^{-2} - 1). \tag{8}$$

Since Y_m is singular at $r = 0$, one must have $B_1 = 0$. The other eigenfunctions readily follow from (5a)–(5d), and one finally obtains

$$\hat{u}(r) = i(\rho\omega_j)^{-1}k^2\beta^{-2}A_1[-2\Omega m r^{-1}\omega_j^{-1}J_m(\beta r) + \beta J_m'(\beta r)], \tag{9a}$$

$$\hat{p}(r) = A_1 J_m(\beta r), \tag{9b}$$

with $J_m'(\beta r) = \partial_x J_m(x)|_{x=\beta r}$.

In the external region $r > R$, the flow is irrotational and one may define a velocity potential Φ such that $\mathbf{u} = \boldsymbol{\nabla}\Phi$, with $\Phi = \varphi(r)e^{i(kz+m\theta-\omega t)}$. The governing equation is $\Delta\Phi = 0$, which, in terms of $\varphi(r)$, reads as

$$r^2\varphi''(r) + r\varphi'(r) - (m^2 + k^2r^2)\varphi(r) = 0. \tag{10}$$

The general solution is $\varphi(r) = A_2 I_m(skr) + B_2 K_m(skr)$, where I_m and K_m are the modified Bessel functions of first and second kind of order $|m|$ and $s \equiv \mathrm{sgn}(k_r)$. Since I_m grows exponentially as $r \to \infty$, one must have $A_2 = 0$. Note that, as $r \to \infty$, $K_m(skr) \sim e^{-skr}/\sqrt{2skr/\pi}$. The sign function s has precisely been introduced in the argument of K_m to ensure that perturbations effectively decay at infinity. The velocity and pressure perturbations are given by

$$\hat{u}(r) = sB_2 k K_m'(skr), \tag{11a}$$

$$\hat{p}(r) = -i\rho[-\omega + \Omega a^2 r^{-2}m + U_\infty k)B_2 K_m(skr)], \tag{11b}$$

with $K_m'(skr) = \partial_x K_m(x)|_{x=skr}$.

Across the vortex sheet $r = R$, continuity of particle displacement and pressure implies that

TABLE I. Low wave number approximations ($k \ll 1$) for axisymmetric ($m=0$) and helical ($m \neq 0$) modes. Here $K \equiv \log(2/sk) - C + 1/4$, where $C = 0.5772$ is the Euler constant, $\mu = \mathrm{sgn}(m)$; $j_{m,n}$ is the nth zero of the Bessel function J_m.

β	$m=0$	$m \neq 0$
$\beta \ll 1$	$\breve{\omega}_0^{\pm} \sim \pm 2S + (1+a)k$	$\breve{\omega}_m \sim (m+2\mu)S + (1+a)k$ $\hat{\omega}_m \sim (m-\mu)S$, if $\lvert m\rvert \neq 1$ $\hat{\omega}_m \sim ak + \mu \frac{k^2}{2}\left(\frac{1}{S} - KS\right)$, if $\lvert m\rvert = 1$
$\beta = \mathcal{O}(1)$	$\omega_{0,n} \sim \left(1 + a + \frac{2S}{j_{0,n}}\right)k + \frac{2Sk}{j_{0,n}}\left(\frac{1}{j_{0,n}} + \frac{1}{2S}\right)^2 k^3 \log(sk)$	$\omega_{m,n} \sim mS + \left(1 + a \pm \frac{2S}{j_{m,n}}\right)k$
$\beta \gg 1$	$\omega_0^{kh} \sim (1+a)k \pm i \frac{k^2 \log(sk)}{2S}$	$\omega_m^{kh} \sim mS + (1+a)k - \mu \frac{k^2}{2S} \pm i \frac{k^3}{2S\lvert m\rvert}$

$$\frac{\hat{u}(R^-)}{\omega_j} = \frac{\hat{u}(R^+)}{\omega_j + \Delta U k}, \tag{12a}$$

$$\hat{p}(R^-) = \hat{p}(R^+). \tag{12b}$$

The above conditions yield two homogeneous algebraic equations for A_1 and B_2 and, in order to obtain a nontrivial solution, one must set the determinant of the system equal to zero. The following linear dimensional dispersion relation is then obtained:

$$[\omega_j + \Delta U k]^2 \left(-2\Omega m \omega_j^{-1} + \beta R \frac{J_m'(\beta R)}{J_m(\beta R)}\right) = -\frac{\omega_j^2 \beta^2 R^2}{skR} \frac{K_m'(skR)}{K_m(skR)}. \tag{13}$$

It is convenient to express (13) in terms of nondimensional parameters by introducing as length and velocity scales the core radius R and the velocity difference ΔU. Without changing notations, relation (13) may then be cast into the dimensionless form

$$D[k,\omega;S,a,m] \equiv (\omega_j + k)^2 \left(-2mS + \omega_j \beta \frac{J_m'(\beta)}{J_m(\beta)}\right) + \frac{\beta^2 \omega_j^3}{sk} \frac{K_m'(sk)}{K_m(sk)} = 0, \tag{14}$$

with

$$\omega_j \equiv \omega - mS - (1+a)k, \tag{15}$$

and

$$\beta \equiv k\sqrt{(4S^2 - \omega_j^2)/\omega_j^2}. \tag{16}$$

In the absence of external flow ($a=0$), one recovers the result of Krishnamoorthy.[21] If, in addition, $S=0$, our results reduce to those calculated by Batchelor and Gill[3] for the plug flow jet.

III. TEMPORAL INSTABILITY ANALYSIS

In this section, the axial wave number k is assumed to be real, and dispersion relation (14) is solved in terms of the complex frequency ω. It is then straightforward to verify that the dependence on external flow parameter a is trivial and amounts to a simple Doppler frequency shift.

Asymptotic solutions of (14) are presented in Sec. III A and compared with numerical results in Sec. III B.

A. Asymptotic results

In the *high wave number regime* $k \gg 1$, one recovers as a leading-order solution of (14) the complex phase velocity,

$$c \equiv \frac{\omega}{k} \sim a + \frac{1 \pm i}{2}. \tag{17}$$

This is the classical result for the Kelvin–Helmholtz instability of a plane vortex sheet (Drazin and Reid[22]). Note that the result is independent of swirl S. In this limit, instability waves are solely controlled by the velocity difference ΔU: they fail to ''see'' the jet curvature and are insensitive to swirl S, at leading order. According to (17), the temporal growth rate $\omega_i \equiv k c_i$ increases linearly with k and there is no high wave number cutoff. Note that causality cannot be enforced since arbitrarily small scales are amplified. Approximation (17) implicitly assumes that β, as defined in (16), becomes infinite with k. If we assume instead $\beta \ll k$ and $k \gg 1$, Eqs. (14)–(16) reduce to

$$\omega \sim (m \pm 2)S + (1+a)k. \tag{18}$$

Such neutral disturbances simply correspond to *inertial waves* propagating in an unbounded medium that is subjected to a solid body rotation.

In the *low wave number regime* $k \ll 1$, one must distinguish the cases $\beta \ll 1$, $\beta = \mathcal{O}(1)$, and $\beta \gg 1$. Leading-order approximations are summarized in Table I for axisymmetric and helical disturbances. According to these results, there exists, *for each azimuthal wave number m*, a single unstable Kelvin–Helmholtz wave ω_m^{kh} and an infinite number of neutral inertial waves $\breve{\omega}_m$, $\hat{\omega}_m$, $\omega_{m,n}$. The neutral modes calculated under the assumption $\beta = \mathcal{O}(1)$ and $\beta \ll 1$ are the analogs of those derived by Moore and Saffman[5] and Saffman[6] for the pure Rankine vortex with no axial flow. The unstable Kelvin–Helmholtz mode ω_m^{kh} obtained when $\beta \gg 1$ does not seem to have been calculated before: it is clearly associated with the presence of axial shear ΔU.

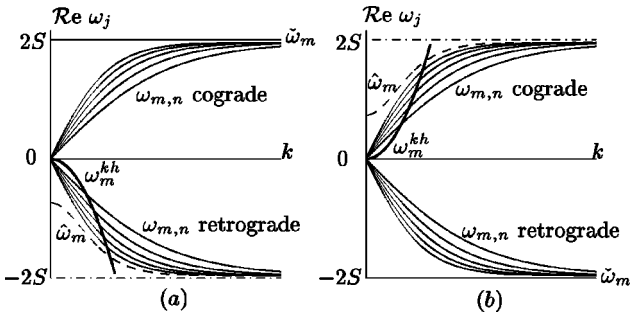

FIG. 3. Sketch of the Doppler shifted frequencies $\mathscr{R}e\ \omega_j(k)$ of inertial modes $\hat{\omega}_m$(− − −), $\check{\omega}_m$ (—), $\omega_{m,n}$ (—) and unstable mode ω_m^{kh} (—). Inertial mode characteristics $\hat{\omega}_m$, $\check{\omega}_m$, and $\omega_{m,n}$ are obtained from Table I and from (19) with $\beta = j_{m,n}$. The asymptotic limit (18) is indicated by (−·−). Unstable mode characteristics ω_m^{KH} are obtained from Table I. (a) $m>0$ and (b) $m<0$.

Saffman[6] suggests that inertial modes be classified according to the sign of the Doppler shifted frequency $\omega_j \equiv \omega - mS - (1+a)k$ observed in a frame of reference moving with the vortex core: a mode is said to be *cograde* if $\omega_j > 0$ and *retrograde* if $\omega_j < 0$. According to (16),

$$\omega_j = \pm \frac{2Sk}{\sqrt{k^2+\beta^2}}. \tag{19}$$

Thus, in the low wave number limit $k \ll 1$, $\beta = \mathscr{O}(1)$, one has (see Table I)

$$\beta \sim j_{m,n}, \ \text{i.e.,} \ \ \omega_j \sim \pm \frac{2Ssk}{j_{m,n}}. \tag{20}$$

We have sketched in Fig. 3 the Doppler shifted frequencies ω_j of the various inertial modes. For the modes $\hat{\omega}_m$, use has been made of the high wave number approximation (18) and the low wave number asymptotic formulas listed in Table I. Approximations to the inertial modes $\omega_{m,n}$ result from the application of relation (19) with $\beta \sim j_{m,n}$. The real part of the unstable Kelvin–Helmholtz mode ω_m^{kh} defined in Table I has also been represented as a thick line. Note that at discrete values $k_{m,n}$ of the wave number, $\mathscr{R}e\ \omega_m^{kh} = \omega_{m,n}$, with $\mathscr{I}m\ \omega_m^{kh} \ll 1$. According to the analytical expressions summarized in Table I, $k_{m,n} \sim \pm 4\mu s S^2 / j_{m,n}$, and, at these wave numbers we expect resonances to take place between the various inertial modes $\hat{\omega}_m$, $\omega_{m,n}$ and the unstable mode ω_m^{kH} induced by the axial shear. Figure 3 indicates that such strong coupling phenomena are likely to involve *retrograde* inertial modes for $m>0$ and *cograde* inertial modes for $m<0$.

The examination of the eigenfunctions obtained in the low wave number limit further confirms the physical nature of the various modes. The pressure distributions $\hat{p}_{m,n}(r)$ and $p_m^{kh}(r)$ pertaining to $\omega_{m,n}$ and ω_m^{kh} can easily be deduced from Eqs. (9b) and (11b) by applying the low wave number approximations of Table I. Typical results are displayed in Fig. 4 for the purely real eigenfunction $\hat{p}_{-1,1}(r)\hat{p}_{-1,2}(r)$ $\hat{p}_{-1,3}(r)$ and for $\mathscr{R}e\ \hat{p}_{-1}^{kh}(r)$ at three different wave numbers $k = 1.1k_{-1,1}$, $1.1k_{-1,2}$, $1.1k_{-1,3}$. The pressure distributions $\hat{p}_{m,n}$ are seen to be confined to the vortex core $r<R$, the number of zero crossings being equal to $n+1$ and the shape

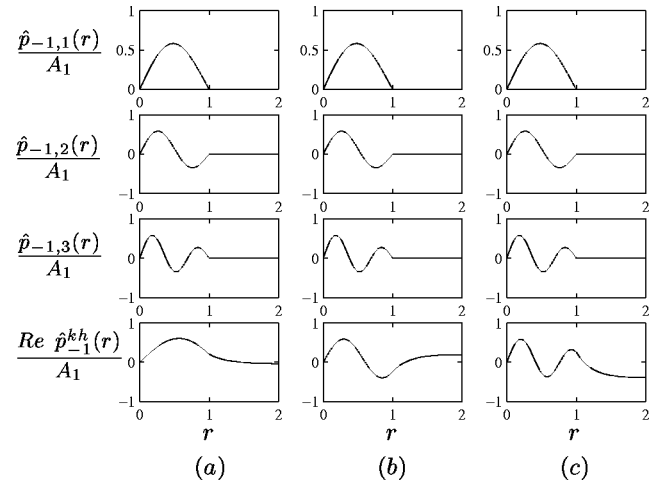

FIG. 4. Evolution of the pressure eigenfunctions $\hat{p}_{-1,1}(r)$, $\hat{p}_{-1,2}(r)$, $\hat{p}_{-1,3}(r)$, $\mathscr{R}e\ \hat{p}_1^{kh}(r)$ with wave number k in the low wave number approximation at $S=0.4$. (a) $k=1.1\ k_{-1,1}$; (b) $k=1.1\ k_{-1,2}$; (c) $k=1.1\ k_{-1,3}$.

remaining invariant with k. This feature demonstrates that the $\omega_{m,n}$'s are indeed waveguide modes composed of inertial waves bouncing off the core boundary $r=R$. By contrast, the pressure distribution $\mathscr{R}e\ \hat{p}_{-1}^{kh}(r)$ of the unstable mode continuously changes with wave number. As k decreases through the resonance points $k_{-1,1}$, $k_{-1,2}$, $k_{-1,3}$, etc., $\mathscr{R}e\ \hat{p}_{-1}^{kh}(r)$ successively takes the shape of $\hat{p}_{-1,1}(r)$, $\hat{p}_{-,2}(r)$, $\hat{p}_{-1,3}(r)$, etc.

According to the general analysis of Leibovich, Brown, and Patel,[23] columnar vortices with arbitrary radial distributions of axial and azimuthal velocity admit an infinite number of branches for each value of the azimuthal wave number m. Furthermore, two types of wave motion may be distinguished. *Slow modes* by definition have zero phase speed $c \equiv \omega/k = 0$ and they only exist for the so-called bending waves $|m| = 1$. Their frequency ω and group velocity $d\omega/dk$ both tend to zero as k goes to zero. *Fast modes*, which by definition have an infinite phase speed, are such that ω tends to $m\Omega(r=0)$ and $d\omega/dk$ tends to a constant as k goes to zero. The results gathered in Table I are entirely consistent with these properties: the only *slow wave* is $\hat{\omega}_m$ obtained for $|m|=1$ and all the $\omega_{m,n}$'s are *fast waves*. Finally $\omega_{m,n} \to mS$ as $k \to 0$.

B. Numerical results

The dispersion relation $D[k,\omega;S,a,m]=0$ defined in (14) may also be solved numerically by making use of standard MATLAB routines. Without loss of generality, the external flow parameter is set equal to $a=0$, the results for $a \neq 0$ being easily deduced from those for $a=0$ by a simple frequency shift $\omega \to \omega - ak$. At a given value of the swirl S, one then seeks to determine all the temporal branches $\omega(k)$, k real, for each azimuthal wave number m. The procedure consists in the following steps: for a given value of S, m, and k, the complex function $D[k,\omega;S,a,m]$ is first calculated at each grid point of a mesh in the complex $\omega_r - \omega_i$ plane, The solutions of $D=0$ are then given by the intersection points of the isolines $\mathscr{R}e\ D=0$ and $\mathscr{I}m\ D=0$. One

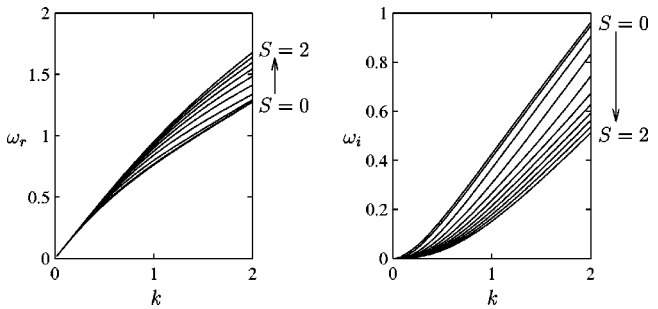

FIG. 5. Temporal instability. Here $a=0$, $m=0$. Real and imaginary parts of frequency $\omega_0^{kh}(k)$ of the unstable Kelvin–Helmholtz mode for different values of swirl S in the range $0\leqslant S\leqslant 2$ with increment $\Delta S=0.2$.

obtains a single complex conjugate pair $\omega_r \pm i\omega_i$ associated with the unstable mode and many neutral modes on the real ω_r axis. These estimates are subsequently used as guess values in a direct solver routine for $D=0$ in order to generate sufficiently accurate numerical values. Solutions for other parameters settings are generated by applying suitable small increments to k and S and proceeding by continuation. Whatever the value of the swirl S, our results confirm that, for each m, there exists a single unstable mode that is the continuation of the pure jet mode isolated by Batchelor and Gill[3] for a plug-flow axial velocity profile with no swirl $S=0$.

1. Axisymmetric mode ($m=0$)

Figure 5 represents the real and imaginary parts of the axisymmetric Kelvin–Helmholtz mode $\omega_0^{kh}(k)$ as the swirl parameter S is increased in the range $0\leqslant S\leqslant 2$. Such unstable disturbances correspond to the formation of vortex rings on the jet column. Swirl is seen to have a stabilizing influence, but all wave numbers remain unstable whatever the value of S. Numerical results are in good quantitative agreement with the low wave number approximation of ω_0^{kh} listed in Table I, as shown in Fig. 6 for a particular value of S.

All other axisymmetric modes $\breve{\omega}_0^{\pm}$ and $\omega_{0,n}$ remain neutrally stable for all k and S. Typical variations of $\breve{\omega}_0(k)$ and $\omega_{0,n}(k)$ are given in Fig. 7.

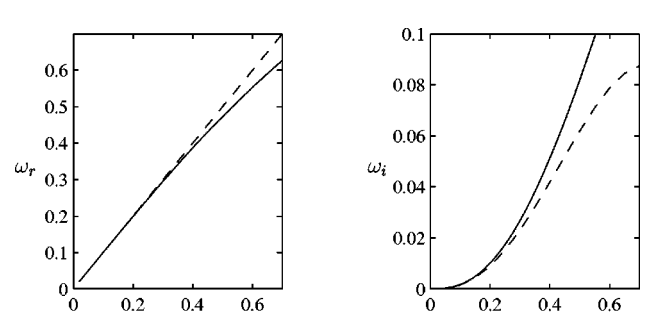

FIG. 6. Temporal instability. Here $S=0.7$, $a=0$, $m=0$. The real and imaginary parts of frequency $\omega_0^{kh}(k)$ of the unstable Kelvin–Helmholtz mode: numerical result (—), low wave number asymptotic formula of Table I (– – –).

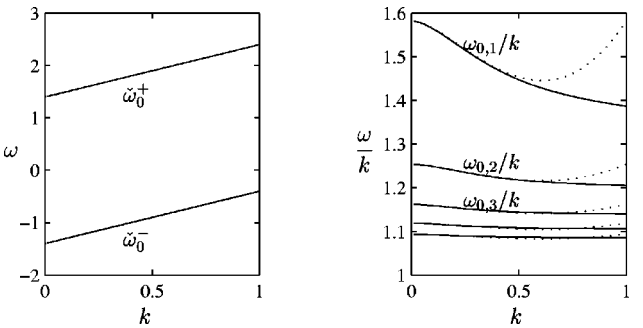

FIG. 7. Here $S=0.7$, $a=0$, $m=0$. Real frequency $\breve{\omega}_0^{\pm}(k)$ and phase velocity $\omega_{0,n}(k)/k$ of neutrally stable inertial modes. The low wave number approximation of Table I (⋯). Note that the low wave number approximation for $\breve{\omega}_0^{\pm}$ corresponds exactly to the numerical calculations.

2. Helical modes ($m\neq 0$)

As soon as a finite amount of swirl is introduced, the reflectional symmetry $\theta\rightarrow -\theta$ is broken and helical modes $+m$ and $-m$, $m\neq 0$, exhibit distinct temporal instability characteristics. Typical examples are illustrated in Fig. 8 for helical bending modes $m=\pm 1$ at two distinct positive swirl settings. In both instances, the negative mode displays a larger growth rate than its positive counterpart on the entire axial wave number range. Extensive numerical surveys indicate that this is always the case. However, this does not mean that all negative helical modes are necessarily more unstable than all positive helical modes. At *low wave numbers*, $\omega_i^{kh}(m;S)$ varies as $1/|m|$, as readily seen from Table I: the most unstable mode is then $m=0$ and the least unstable is $|m|=\infty$. At *high wave numbers*, ω_i $(m;S>0)$ is numerically determined to decrease continuously with increasing m: $m=-\infty$ is then the most unstable. In the sequel, we discuss the case of the negative bending mode $m=-1$.

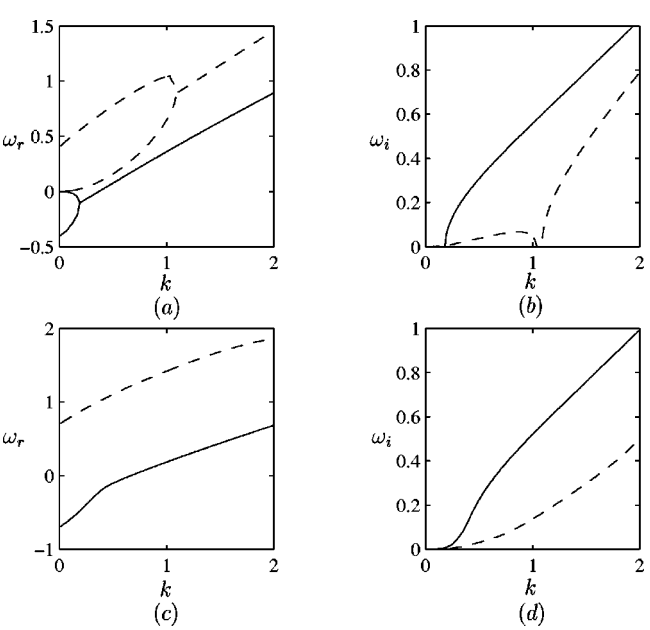

FIG. 8. Temporal instability: $a=0$, $m=\pm 1$. Real and imaginary parts of unstable Kelvin–Helmholtz frequencies $\omega_{-1}^{kh}(k)$ (—) and $\omega_1^{kh}(k)$ (– – –) at different swirl values S. (a) and (b) $S=0.4$; (c) and (d) $S=0.7$.

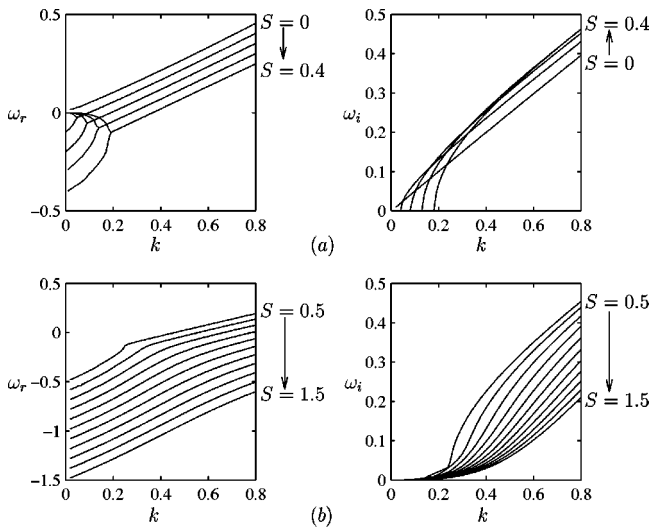

FIG. 9. Temporal instability: $a=0$, $m=-1$. Real and imaginary parts of frequency $\omega_{-1}^{kh}(k)$ of the unstable Kelvin–Helmholtz mode for different values of swirl S. (a) $0\leqslant S\leqslant 0.4$; infinitely many neutral bands appear in wave number interval $0\leqslant k\leqslant K(S)$ (see Figs. 10 and 11). (b) $0.5\leqslant S\leqslant 1.5$: temporal growth rate ω_i decreases with increasing swirl but all wave numbers k remain unstable.

The temporal instability characteristics of the unstable Kelvin–Helmholtz mode $m=-1$ are displayed in Fig. 9: the real and imaginary parts of the frequency $\omega_{-1}^{kh}(k)$ are represented for increasing swirl in the range $0\leqslant S\leqslant 1.5$. From these graphs, one may infer that increasing swirl has a different effect on the unstable mode in the two distinct subranges $0\leqslant S\leqslant S_c$ and $S\geqslant S_c$, where $S_c(m=-1)=0.46$. In the range $S\geqslant S_c$ [Fig. 9(b)], increasing S decreases the temporal growth rate ω_i of all axial wave numbers, which, nonetheless, remain unstable for all S. When $S\leqslant S_c$ [Fig. 9(a)], increasing S appears at first glance to stabilize low wave numbers in a wider and wider range $0\leqslant k\leqslant K(S)$ while high wave numbers are slightly destabilized. The same general trend is observed for higher-order positive and negative helical modes. However, positive helical mode growth rates monotonically decrease with increasing swirl in the high wave number range. A closer examination of the low wave number range reveals that the situation is far more complex, as evidenced in (Figs. 10, 11, and 12.)

As soon as a small amount of swirl is applied, a very peculiar set of bubble-like structures appears in a finite wave number band $0\leqslant k\leqslant K(S)$. For a given S, any $k\geqslant K(S)$ is unstable, while the range $0\leqslant k\leqslant K(S)$ exhibits a sequence of bubbles of instability [solid curves in Figs. 10(a), 11(a)] separated by small wave number bands of neutral stability. The transition wave number $K(S)$ between these two regimes gradually increases with S. Infinitesimal bubbles of instability appear as soon as S differs from zero. When S increases toward $S_c(m=-1)\equiv 0.46$, the wave number extent of each unstable bubble widens and neutral bands gradually shrink [compare Figs. 10(a) and 11(a)]. Concurrently, the temporal growth rate envelope decreases continuously with increasing swirl S. At the limiting value $S=S_c$, contiguous bubbles occupy the entire segment $0<k<K(S_c)$ and

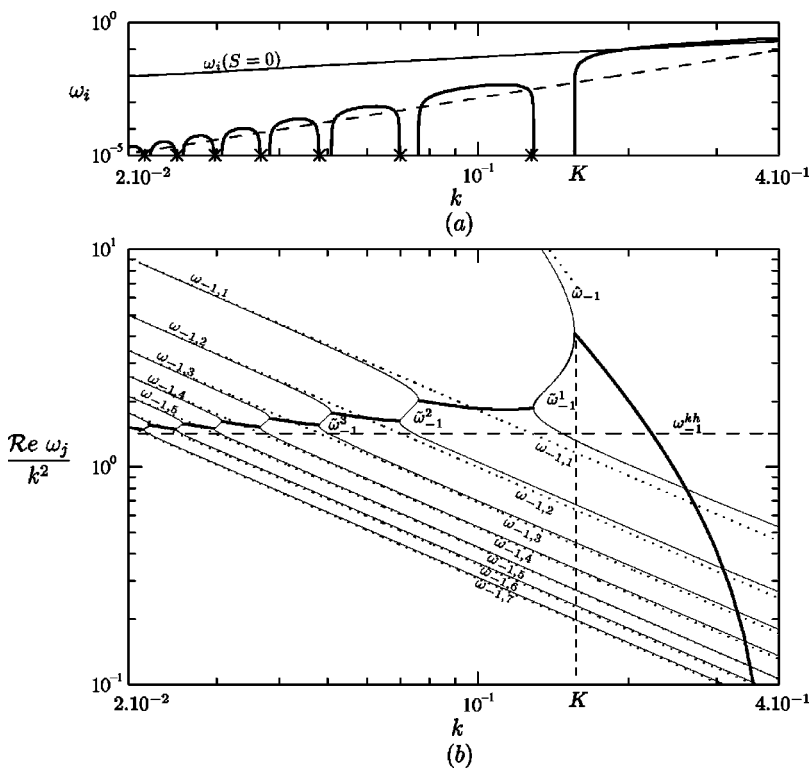

FIG. 10. Temporal instability at low wave numbers. Here $S=0.35<S_c$, $a=0$, $m=-1$. (a) Temporal growth rate $\omega_i(k)$ of the unstable Kelvin–Helmholtz mode (– – –) and comparison with a low wave number approximation for $\omega_{-1}^{kh}(k)$ of Table I (– – –). Resonance wave numbers (×) $k_{m,n}\sim 4S^2/j_{m,n}$ calculated in Sec. III A. (b) The real part of $\omega_j(k)/k^2$ versus wave number k; unstable band (—); neutral band (—); the low wave number approximation for $\omega_{-1}^{kh}(k)$ of Table I (– – –); the low wave number approximation for $\hat{\omega}_{-1}(k)$, $\omega_{-1,n}(k)$ of Table I (– – –).

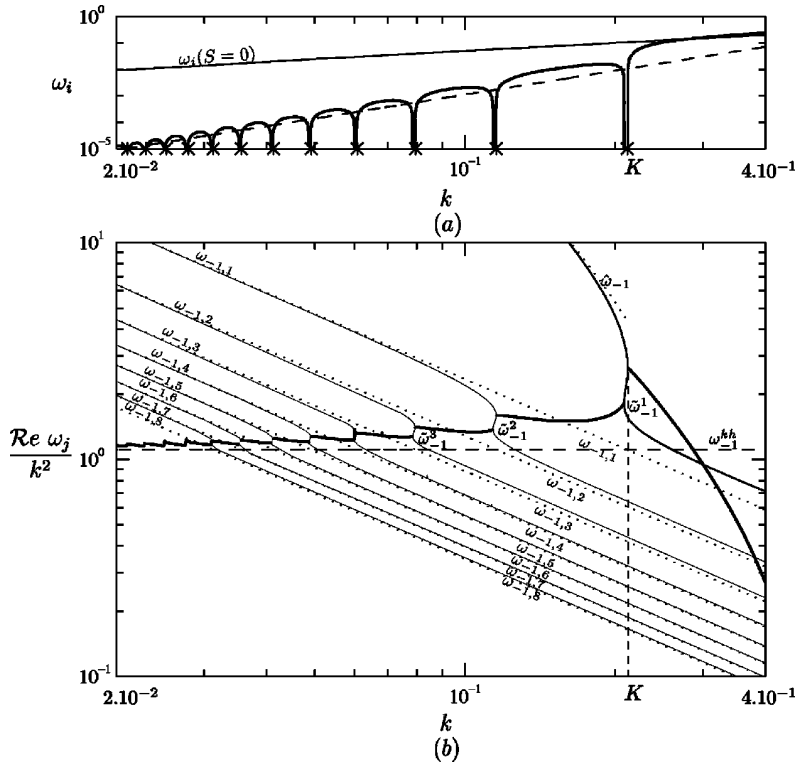

FIG. 11. Temporal instability at low wave numbers. Here $S=0.45<S_c$, $a=0$, $m=-1$. The same quantities as in Fig. 10.

neutral bands reduce to separation points. Finally, as S exceeds S_c [Fig. 12(a)], all bubbles ''burst'' and merge to yield a single regime of unstable wave numbers throughout. The low wave number approximation for the growth rate $\mathcal{I}m\ \omega_m^{kh}$ deduced from Table I [dashed curves in Figs. 10(a), 11(a), 12(a)] is seen to provide a leading-order estimate of the envelope of the bubbles or their remnants.

In order to understand the generation mechanism responsible for bubble formation, it is enlightening to examine the corresponding variations of the real parts ω_r [Figs. 10(b),

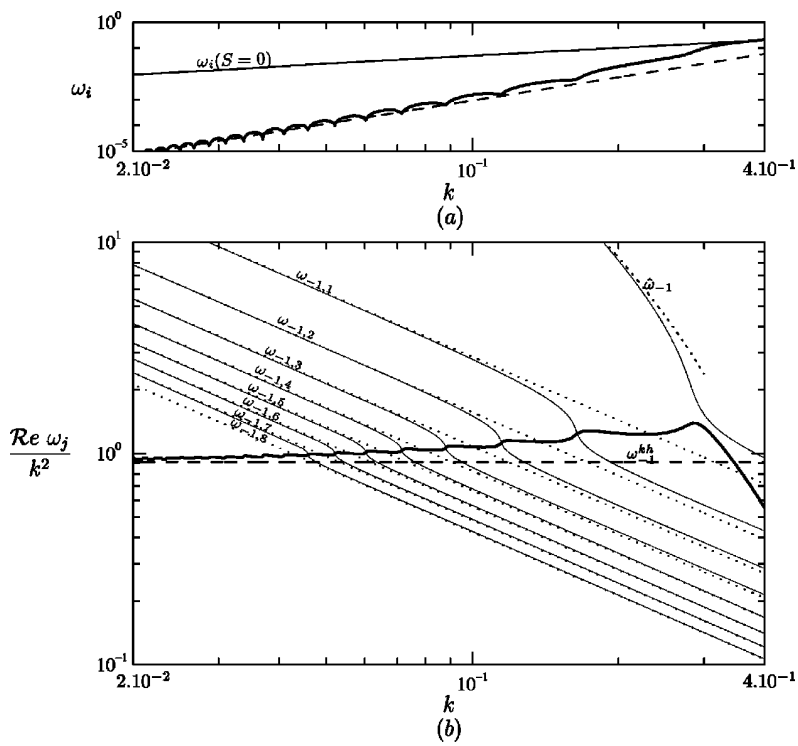

FIG. 12. Temporal instability at low wave numbers. Here $S=0.55>S_c$, $a=0$, $m=-1$. The same quantities as in Fig. 10.

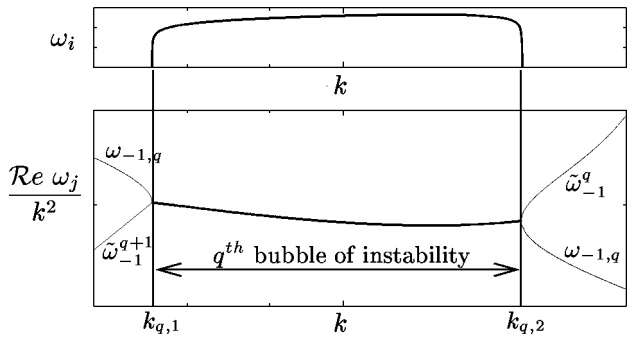

FIG. 13. Sketch of resonance interactions giving rise to a generic qth bubble of instability. (a) Temporal growth rate $\omega_i(k)$. (b) The real part of $\omega_j(k)/k^2$ versus wave number k. The same notation as in Fig. 10(b).

11(b), 12(b)] in the scaled form $\mathcal{R}e\ \omega_j/k^2$ vs k, where ω_j is the Doppler-shifted frequency defined in (15). Low wave number approximations listed in Table I for $\omega_m^{kh}(k)$ (dashed lines) and $\hat{\omega}_m(k)$, and $\omega_{m,n}(k)$ (dotted lines) have also been represented on each figure. The agreement between the asymptotic formulas and numerical results is seen to be satisfactory. Furthermore, low wave number approximations provide a convenient means of labeling the various stable (thin solid lines) and unstable (thick solid lines) branches appearing in Figs. 10(b), 11(b), 12(b).

These plots reveal the widespread occurrence of direct resonances between the unstable Kelvin–Helmholtz mode ω_m^{kh} and the various neutrally stable inertial modes $\hat{\omega}_m$ and $\omega_{m,n}$. The nature of the interactions giving rise to a generic qth bubble of instability is sketched in Fig. 13, where it is understood that q increases with decreasing bubble size, $q=1$ denoting the largest bubble located just on the left of $k=K(S)$. Let $k_{q,1}$ and $k_{q,2}>k_{q,1}$ designate the lower and upper limits of the qth bubble. At the lower end $k=k_{q,1}$ of the qth bubble, the neutral inertial mode $\omega_{m,q}$ merges with a neutral mode noted $\tilde{\omega}_m^{q+1}$ to give rise to an unstable band. Similarly, at the upper end $k=k_{q,2}$ of the qth bubble, the unstable Kelvin–Helmholtz mode resonates with the neutral inertial wave $\omega_{m,q}$ and splits into two neutral waves $\omega_{m,q}$, and $\tilde{\omega}_m^q$ above $k_{q,2}$. Finally, $\tilde{\omega}_m^1$ merges with $\hat{\omega}_m$ at $k=K$ to give rise to the unstable mode ω_m^{kh} for all k.

This interpretation is further corroborated by the fact that the resonance wave numbers $k_{m,n}\sim 4S^2/j_{m,n}$ defined by $\mathcal{R}e\ \omega_m^{kh}=\omega_{m,n}$ and estimated in Sec. III A, provide an excellent approximation to $k_{q,2}$, as indicated by the crosses on the k axis of Figs. 10(a) and 11(a). In Figs. 9–13, we have chosen to illustrate the typical behavior of helical modes $m<0$ that results from the resonances anticipated in Fig. 3(b). A similar phenomenology arising from the resonances present in Fig. 3(a) prevails for helical modes $m>0$. It is not illustrated here for the sake of brevity. Thus, when $m<0$ $(m>0)$, all the cograde (resp., retrograde) neutral inertial modes $\omega_{m,q}$ induced by swirl successively interact with the Kelvin–Helmholtz mode to alternatively produce neutral wave number bands and bubbles of instability. To the infinite countable set of neutral inertial waves is associated an infinite countable set of bubbles of instability that become smaller and smaller in size as k tends to zero. The unstable mode for the Rankine vortex with axial flow is in fact a coupled mode involving interactions between the pure unstable Kelvin–Helmholtz mode of the plug flow jet[3] and the neutral inertial waves supported by the Rankine vortex.[4–6] Finally, note that, when $S>S_c$ (Fig. 12), the above interactions are not capable of producing neutral bands but they still significantly affect the behavior of the unstable mode, as evidenced by the bumps in Fig. 12(a) and the undulations in Fig. 12(b).

IV. ABSOLUTE/CONVECTIVE INSTABILITY

If, as mentioned in Sec. III B, the effect of the external flow parameter a on the evolution of temporal waves (k real, ω complex) can be accounted for by a simple Doppler frequency shift $\omega\rightarrow\omega-ak$, such is not the case for spatial waves (k complex, ω real) and more generally spatiotemporal waves (k complex, ω complex).

We now proceed to investigate the absolute/convective nature of the instability in the Rankine vortex with axial flow in $a-S$ control parameter space. More specifically, we seek to determine the transition curves $a_c(S;m)$ separating the regions of absolute and convective instability for different azimuthal wave numbers m. According to a well-established criterion (see Huerre and Monkewitz[1] for a review), the absolute/convective nature of the instability is ascertained by studying the behavior of spatial branches in the vicinity of saddle points (k_0,ω_0) of the dispersion relation (14) in the complex k plane, given by

$$D[k_0,\omega_0;a,S,m]=0, \tag{21a}$$

$$\partial_k D[k_0,\omega_0;a,S,m]=0, \tag{21b}$$

$$\partial_\omega D[k_0,\omega_0;a,S,m]\neq 0. \tag{21c}$$

In order to qualify as *the complex absolute wave number* k_0 and *frequency* ω_0,[24] the saddle point k_0 must involve pinching of two distinct spatial branches $k_m^+(\omega)$ and $k_m^-(\omega)$, which, for large enough $\omega_i>0$, are initially confined to their respective half k planes $k_i>0$ and $k_i<0$. Such branches are commonly referred to as upstream and downstream branches, respectively, and $\omega_{0,i}=\mathcal{I}m\ \omega_0$ as the absolute growth rate. If $\omega_{0,i}>0$ $(\omega_{0,i}<0)$, the flow is said to be absolutely (convectively) unstable for the particular azimuthal wave number m under consideration, the transition curve $a_c(S;m)$ being given by $\omega_{0,i}=0$. In order to conclude as to the overall absolute/convective nature of the instability for particular settings of a and S, the analysis must be repeated for various azimuthal wave numbers m.

A. General procedure

In practice, the method follows the steps illustrated in Fig. 14. For given a, S, and m, the downstream spatial branch $k_m^+(\omega)$ is retrieved by exploiting the fact that any point on the unstable temporal branch $\omega_m^{kh}(k)$ calculated in Sec. III also belongs to $k_m^+(\omega)$. To such a point indicated by a star in the complex k plane of Fig. 14(a), correspond known values of ω_r and $\omega_i>0$. The $\omega_i=$const curve passing through this point is by definition the locus of $k_m^+(\omega)$ as ω travels along the corresponding $\omega_i=$const horizontal line in

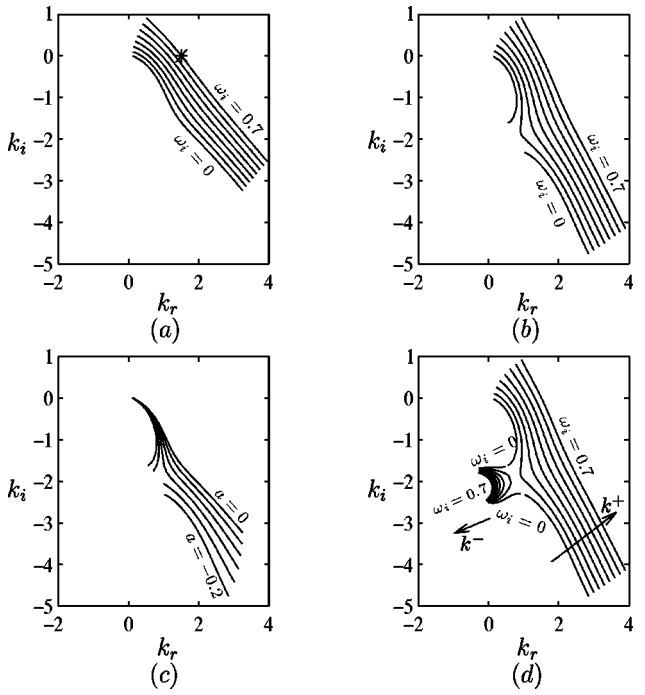

FIG. 14. Illustrative loci of spatial branches $k(\omega)$ in the complex k plane for $m=0$, $S=0$. (a) $a=0$, loci of $k(\omega)$ as ω_i decreases from 0.7 to 0 in 0.1 increments. The $*$ symbol denotes the starting point on the k_r axis obtained from temporal stability calculations of Sec. III. Convective instability. (b) $a=-0.2$, loci of $k(\omega)$ as ω_i decreases from 0.7 to 0 in 0.1 increments. Absolute instability. (c) $\omega_i=0$, loci of $k(\omega)$ as a decreases from 0 to -0.2 in 0.04 increments. A saddle point appears for $a=-0.154$. (d) $a=-0.2$; loci of $k(\omega)$ as ω_i increases from 0 to 0.7 in 0.1 increments. The interacting branch is indeed a k^--type that recedes into the lower half-k plane.

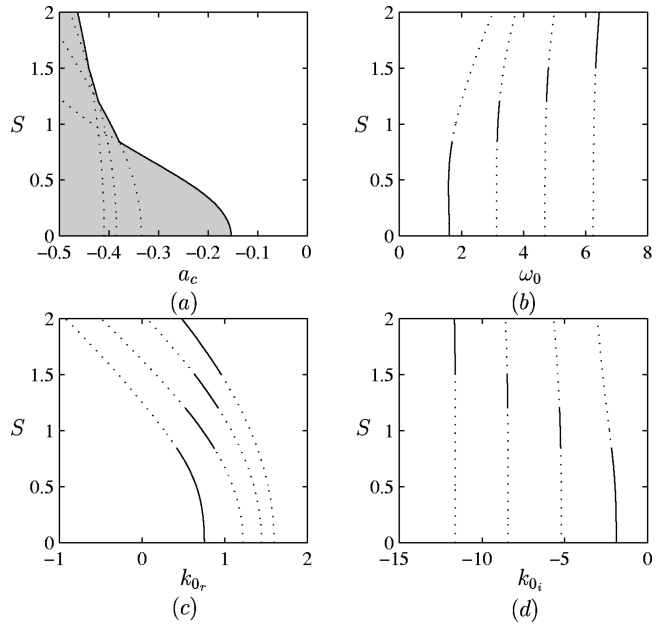

FIG. 15. Absolute/convective transition of an axisymmetric mode ($m=0$) for jet-like velocity profiles ($a>-0.5$). Solid (dotted) lines denote results pertaining to dominant (subdominant) saddle points. Shaded (clear) areas denote absolute (convective) instability. (a) Transitional external flow $a_c(S;0)$ versus swirl S. (b) Absolute frequency ω_0 vs S along the transition curve. (c) The real part $k_{0,r}$ of absolute wave number versus S along the transition curve. (d) The imaginary part $k_{0,i}$ of absolute wave number versus S along the transition curve.

the complex ω plane. This curve can be reconstructed by keeping ω_i constant, varying ω_r in small increments and calculating corresponding complex values of $k_m^+(\omega)$. The deformations of the locus $k_m^+(\omega)$ may be followed by continuation as ω_i is decreased in small increments. Typical results are displayed in Figs. 14(a) and 14(b). If, as ω_i decreases from positive values toward zero, no saddle point happens to be encountered [the case of Fig. 14(a)], one must conclude that, for the selected values of a, S, and m, the instability is convective. If, in the same process, a saddle point is encountered [the case of Fig. 14(b)], the instability is absolute. In order to locate the absolute/convective transition point $a_c(S;m)$ for given S and m, the deformations of the spatial branch $k_m^+(\omega)$ corresponding to $\omega_i=0$ are monitored as a is decreased from the reference value $a=0$ in Fig. 14(a). In the case of Fig. 14(c), a saddle point has been detected as a crosses the critical value $a_c=-0.15$. To verify that this saddle point indeed involves an interaction between a k^+ and a k^- branch, the external flow parameter a is then kept at the critical value a_c or at a slightly higher value and the deformations of the spatial branches are followed as ω_i is increased away from zero. A typical result is shown in Fig. 14(d): the interacting branch has been generated at $\omega_i=0$ by continuation and, as ω_i increases, one clearly distinguishes the k_m^+ branch that migrates toward the upper half-k plane and the interacting k_m^- branch that recedes into the lower half-k plane. The transition value $a_c(S;m)$ has therefore been determined for given settings of S and m and the associated saddle point k_0 complex and ω_0 real has been located. For each azimuthal wave number m, the procedure is initiated at the reference values $S=0$, $a=0$. This configuration, that corresponds to a plug-flow jet profile with no external flow and no swirl, is known to be convectively unstable.

The variations of $a_c(S;m)$ and the trajectory of the saddle point k_0 complex, ω_0 real right at the absolute/convective transition may then be followed, as S is increased from the previous reference value, by solving (21a)–(21c) for $k_{0,r}$, $k_{0,i}$, ω_0 real, and a_c. In such a fashion, the absolute/convective transition curves $a_c(S;m)$ and the associated complex absolute wave number $k_0(S;m)$ and real absolute frequency $\omega_0(S;m)$ may be calculated both for *jet-like* ($a>-0.5$) and *wake-like* ($a<-0.5$) configurations.

In the following two sections (Sec. IV B, Sec. IV C), we mainly focus our attention on the peculiar properties displayed by the absolute/convective transition in jets ($a>-0.5$). Corresponding results for wakes ($a<-0.5$) are discussed in Sec. IV D.

B. Absolute/convective transition of axisymmetric modes ($m=0$) in jets ($a>-0.5$)

The variations of the transitional external flow $a_c(S;0)$ and of corresponding values ω_0, $k_{0,r}$ and $k_{0,i}$ are presented in Fig. 15, for jet-like configurations ($a>-0.5$). Domains of convective ($a>a_c$) and absolute ($a<a_c$) instability in the a-S parameter plane are displayed in Fig. 15(a). In the absence of swirl ($S=0$), the plug-flow jet becomes absolutely unstable to axisymmetric disturbances at the critical counter-

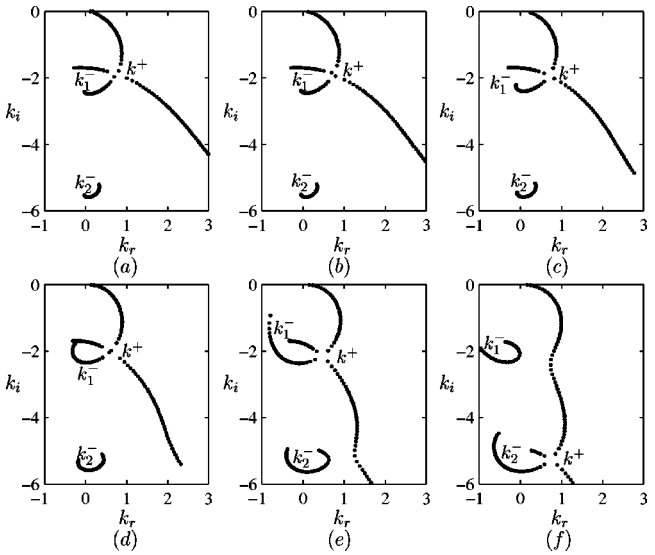

FIG. 16. The configuration of spatial branches $k^+(\omega)$ and $k^-(\omega)$ for selected values of swirl S along the axisymmetric transition curve $a_c(S;0)$ in Fig. 15(a). All contours correspond to $\omega_i=0$. (a) $S=0$; (b) $S=0.2$; (c) $S=0.4$; (d) $S=0.6$; (e) $S=0.8$; (f) $S=1$.

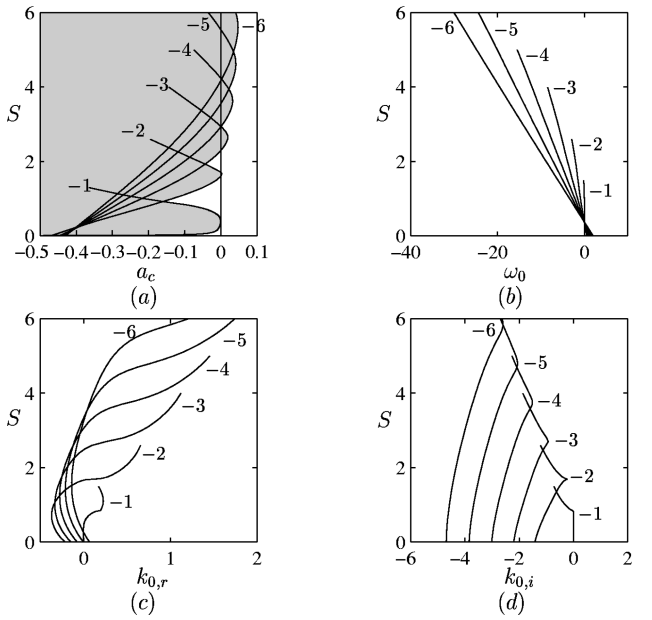

FIG. 17. Absolute/convective transition of the negative helical modes ($m<0$) for jet-like velocity profiles ($a>-0.5$). Shaded (clear) areas denote absolute (convective) instability. (a) Transitional external flow $a_c(S;m)$ vs S. (b) Absolute frequency ω_0 vs S along the transition curve. (c) The real part $k_{0,r}$ of absolute wave number vs S along the transition curve. (d) The imaginary part $k_{0,i}$ of absolute wave number vs S along the transitional curve.

flow $a_c(0;0)=-0.15$. The amount of counterflow necessary to trigger an absolute instability of the $m=0$ mode significantly increases with the swirl S.

The transition curve $a_c(S;0)$ in Fig. 15(a) exhibits several discontinuities in slope. As seen in Figs. 15(b)–15(d), such features are clearly associated with ubiquitous jumps in the variations of ω_0, $k_{0,r}$, and $k_{0,i}$, as S crosses specific values. In order to understand this peculiar behavior, the configuration of pertinent spatial branches $k^+(\omega)$ and $k^-(\omega)$ has been represented in Fig. 16, for selected values of the swirl S along the transition curve of Fig. 15(a). As long as $S\leqslant 0.8$ [Figs. 16(a)–16(e)], the critical saddle point at transition [the solid segment in Figs. 15(b)–15(d)], involves the pinching of the *same* spatial branches $k^+(\omega)$ and $k_1^-(\omega)$. As S reaches unity [Fig. 16(f)], the critical saddle point at transition shifts discontinuously: it now involves pinching of the spatial branch $k^+(\omega)$ with another upstream branch $k_2^-(\omega)$. The former saddle point has become subdominant and it is represented by dotted lines in Figs. 15(b)–15(d). Correspondingly, the transition curve $a_c(S;0)$ shifts discontinuously in order to follow the dominant saddle point. This phenomenon occurs repeatedly as $k^+(\omega)$ interacts with successive $k^-(\omega)$ branches for increasing values of S.

According to the diagram of Fig. 15(a), it must be concluded that *axisymmetric modes cannot induce a transition to absolute instability unless a sufficiently strong counterflow* $a<0$ *is applied*.

C. Absolute/convective transition of helical modes ($m\neq 0$) in jets ($a>-0.5$)

The family of saddle points described in the previous section also exists for all helical modes $m\neq 0$. As discussed in the sequel, negative helical modes $m<0$ are found to admit an additional family of saddle points that is much more ''effective'' in triggering a transition to absolute instability, *even in the absence of axial counterflow*.

The transitional external flow $a_c(S;m)$ for this second family of saddle points pertaining to jet-like velocity profiles ($a>-0.5$) and corresponding values of ω_0, $k_{0,r}$, and $k_{0,i}$, are displayed in Fig. 17, as a function of swirl S, for different negative azimuthal wave numbers m.

Domains of absolute and convective instability for this second family of saddle points are shown in Fig. 17(a). In the absence of swirl ($S=0$), the plug-flow jet becomes absolutely unstable to negative helical modes only for large counterflows $a_c(0,\pm 1)=-5.24$, $a_c(0,\pm 2)=-0.47$, $a_c(0,\pm 3)=-0.45$, etc. As the swirl S is increased, the amount of axial counterflow $|a_c|$ necessary to trigger an absolute instability drastically decreases before increasing for large values of the swirl. Jets with weak coflow ($a>0$) are, in fact, able to sustain a pocket of absolute instability for sufficiently strong swirl S, the transitional azimuthal wave number m increasing regularly in magnitude with S.

The absolute frequency ω_0 along each transitional curve is seen to decrease linearly with increasing swirl S [Fig. 17(b)]. Furthermore, the variations of the complex absolute wave number k_0 with swirl S display qualitatively similar features for all helical modes, as evidenced in Figs. 17(c) and 17(d).

It is worth analyzing in more detail the results pertaining to zero external flow jets ($a=0$). Quantitative estimates of the range of swirl parameters for which a given helical mode m is absolutely unstable are displayed in Fig. 18: the lower and upper values $S_1(|m|)$ and $S_2(|m|)$ defining the limits of

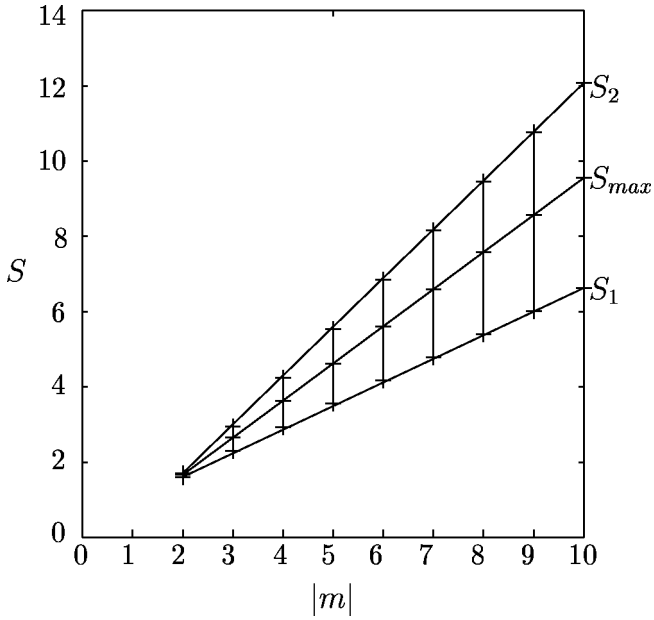

FIG. 18. Absolutely unstable domain in the $|m|-S$ plane for jets with zero external flow ($a=0$). The lower and upper limits $S_1(|m|)$ and $S_2(|m|)$, of absolute instability, on the vertical axis $a=0$ of Fig. 17(a) vary linearly with $|m|$. The swirl values $S_{\max}(|m|)$ at the tips of the transition parabolas $a_c(S;m)$ in the half-plane $a>0$ of Fig. 17(a) also fall on a straight line.

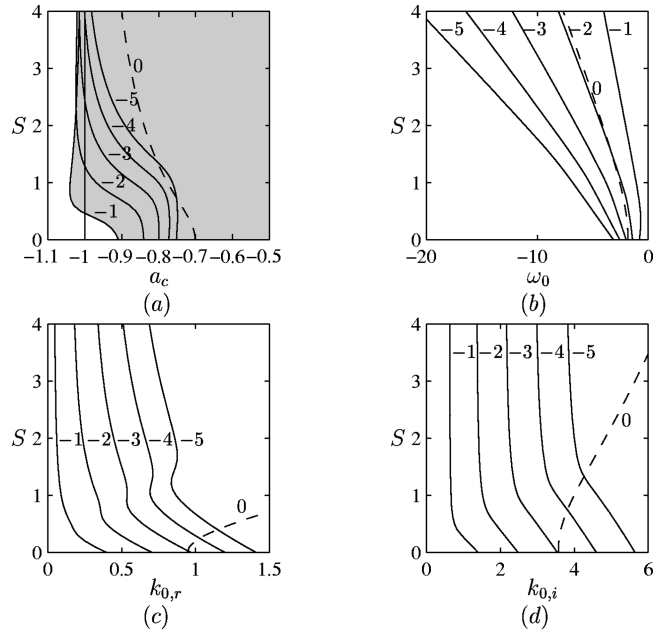

FIG. 19. Absolute/convective transition of axisymmetric ($m=0$) and negative helical modes ($m<0$) for wake-like velocity profiles ($a<-0.5$). Shaded (clear) areas denote absolute (convective) instability. (a) Transitional external flow $a_c(S;m)$ versus swirl. (b) Absolute frequency ω_0 vs S along the transition curve. (c) The real part $k_{0,r}$, of the absolute wave number versus S along the transition curve. (d) The imaginary part $k_{0,i}$ of absolute wave number versus S along the transition curve.

the absolutely unstable ranges for the zero external flow jet [$a=0$, the vertical axis of Fig. 17(a)] have been drawn as a function of azimuthal wave number $|m|$. The value $S_{\max}$ of the swirl associated with the maximum of $a_c(m;S)$ over S [the tip of the parabolas in Fig. 17(a)] has also been represented as a function of $|m|$ on the same plot, even though it does not strictly pertain to the zero external flow case. According to Figs. 17(a) and 18, the jet with no external flow ($a=0$) is seen to remain convectively unstable below $S=1.61$. Note that, according to Fig. 17(a), the mode $m=-1$ only undergoes an effective transition to absolute instability if $a<0$, i.e., in the presence of a finite counterflow. As S exceeds the critical value $S=1.61$, the plug-flow jet first becomes absolutely unstable with respect to the helical mode $m=-2$, and it remains so in the range $1.61<S<1.71$. In the swirl interval $1.71<S<2.30$, the jet becomes convectively unstable again. Beyond $S=2.30$, the flow remains absolutely unstable for all S and the number of absolutely unstable helical modes increases regularly with swirl S within a wedge-like region bounded by the two effectively straight lines $S_1(|m|)$ and $S_2(|m|)$. The computed values of $S_{\max}$ also fall on a straight line lying within the wedge. As seen in Fig. 17(a), the large number of absolutely unstable helical modes for large S is due to increasing overlap between the regions of absolute instability pertaining to each value of m.

D. Absolute/convective transition in wakes ($a<-0.5$)

The absolute/convective transition curves for both axisymmetric ($m=0$) and negative helical modes ($m\neq 0$) may simply be obtained for arbitrary swirl values by tracking the single saddle point emerging from the absolute/convective transition point $a_c(0;m)$ for zero swirl. The resulting transitional external flow $a_c(S;m)$ and corresponding values of ω_0, and $k_{0,r}$, and $k_{0,i}$ are displayed in Fig. 19, as a function of swirl S, for different azimuthal wave numbers.

Domains of absolute and convective instability are shown in Fig. 19(a). In the absence of swirl ($S=0$), the plug-flow coflowing wake [$a\leqslant -1$, as in Fig. 2(b)] is always convectively unstable. For sufficiently large counterflow $1+a>0.091$ within the core [as in Fig. 2(c)], the wake is seen to become absolutely unstable to helical modes $m=\pm 1$. Critical values of the external flow parameter correspond to $a_c(0;\pm 1)=-0.91$, $a_c(0;\pm 2)=-0.84$,..., for successively higher values of $|m|$. As the swirl S is increased, the amount of core counterflow $1+a$ necessary to trigger an absolute instability decreases very significantly. Just as in the case of jets, coflowing wakes ($a\leqslant -1$) are indeed capable of sustaining a pocket of absolute instability for sufficiently large swirl $S>0.47$. The transitional azimuthal wave number remains equal to $m=-1$ until $S=2.32$. For still larger swirl, it successively takes higher negative integer values $m=-2$, $m=-3$, etc.

The absolute frequency ω_0 along the transition curve for each azimuthal wave number m decreases regularly with increasing swirl S [Fig. 19(b)]. Variations of the complex absolute wave number k_0 with S display similar features for all $m<0$, as illustrated in Figs. 19(c) and 19(d).

As a typical example, let us examine the effect of swirl on the zero core velocity wake $a=-1$. According to Fig. 19(a), it is convectively unstable for zero swirl and remains so below the critical value $S_c=0.47$. Above this value, it becomes absolutely unstable with respect to the helical mode $m=-1$ and remains absolutely unstable thereafter. As S in-

creases to larger and larger values, higher-order helical modes $m=-2$, $m=-3$,..., successively undergo a transition to absolute instability within strongly overlapping intervals of S.

V. DISCUSSION AND CONCLUSIONS

The temporal instability properties of the Rankine vortex with an axial plug-flow velocity profile have been determined as a function of swirl parameter S. The axisymmetric mode ($m=0$) remains unstable for all axial wave numbers, but growth rates continuously decrease with increasing S. The introduction of a finite amount of swirl breaks the reflectional symmetry with respect to the transformation $\theta\rightarrow-\theta$, which results in distinct temporal instability properties for helical modes $+m$ and $-m$. At a given $|m|$, positive swirl leads to larger growth rates for $m<0$ than for $m>0$. However, the more unstable negative helical modes do not necessarily exhibit larger growth rates when compared with the zero swirl case. *In the low wave number range*, small amounts of swirl lead to the formation of infinitely many bubbles of instability separated by neutrally stable wave number bands. The growth rate envelope decreases continuously with increasing swirl and neutrally stable bands vanish beyond a critical swirl value. *In the high wave number range*, low swirl levels are destabilizing and large ones are stabilizing for negative helical modes ($m<0$). For positive helical modes, increasing swirl is always stabilizing. Note that high axial wave numbers always remain unstable. These general trends, namely the stabilizing effect of swirl on positive helical modes, its destabilizing effect on negative helical modes for moderate swirl levels, are consistent with earlier instability analyses of fully developed swirling jet profiles (Lessen and Paillet,[9] Lessen, Singh, and Paillet,[10] Khorrami,[11] and Khorrami[15]). Note, however, that the present necessarily inviscid framework is incapable of capturing the weakly amplified viscous modes identified by Khorrami.[11]

According to the above conclusions, the temporal instability behavior does not lead to a clear cut determination of the most unstable azimuthal mode. Absolute/convective instability considerations are in fact much more effective in discriminating between the various eigenmodes, as discussed below. The AI/CI transition pertaining to jets [$a>-0.5$, Figs. 15(a) and 17(a)] and wakes [$a<-0.5$, Fig. 19(a)] have been combined in Fig. 20 to yield a comprehensive picture of the AI domain in the a-S parameter plane for all values of the external flow parameter a. The most striking feature of this state diagram resides in the fact that only axisymmetric and negative helical modes are involved in defining the transition boundary of the AI region.[25] Furthermore, the magnitude of the transitional mode index increases continuously with swirl parameter S on both jet ($a>-0.5$) and wake ($a<-0.5$) sides. Concurrently, the a interval of AI is significantly wider for swirling jet ($S\neq0$) than for nonswirling jets ($S=0$). On the jet side, the AI/CI boundary takes the shape of overlapping tongues pertaining to distinct negative helical modes. On the wake side, the boundary is much smoother, higher-order negative helical modes gradually taking over to

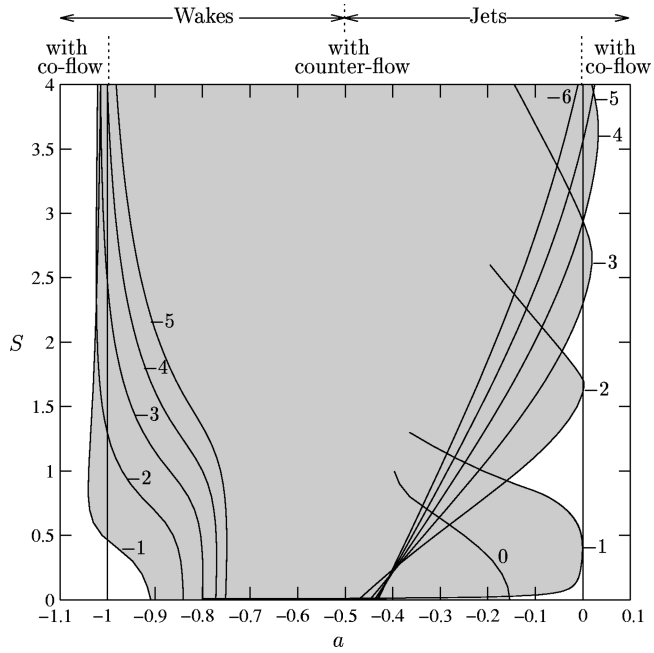

FIG. 20. Absolute/convective instability domains in the a-S parameter plane for jets and wakes. Shaded (clear) areas denote absolute (convective) instability.

define the transition curve for large swirl. For zero swirl, jets/wakes are AI only for sufficiently large counterflow in the range $-0.91<a<-0.15$, the lower bound pertaining to the bending mode $m=-1$ for wakes and the upper bound to the axisymmetric mode $m=0$ for jets. As S increases, the transitional mode $m=0$, on the jet side, is almost immediately superceded by the bending mode $m=-1$. When the swirl parameter reaches the value $S=0.43$, the tip of the $m=-1$ tongue barely fails to touch the $a=0$ axis and swirling jets are then AI to the $m=-1$ mode for a minimum external counterflow amount $a=-10^{-4}$. The $m=-2$ tongue penetrates into the coflowing jet side $a>0$ in the range $1.61<S<1.71$, thereby first leading to AI. Beyond $S=2.30$, weak coflow jets may exhibit AI with respect to higher-order helical modes $m=-3$, -4, etc. On the wake side, AI may take place for coflowing wakes ($a<-1$) as soon as swirl exceeds the value $S=0.47$.

The shape of the AI domain is qualitatively similar to its counterpart for the Batchelor vortex.[12,13] In both instances, swirl strongly promotes AI, which sets in via negative helical modes of varying order and makes it possible for coflowing jets and wakes to undergo AI. On the wake side of the Batchelor vortex, the transitional mode is primarily $m=-1$, as in the present case. On the jet side of the Batchelor vortex, AI successively takes place via $m=-1$, -2, -3, -2, -1, as swirl increases. The $m=0$ mode is then irrelevant since it is stable. Finally, in contrast with the plug-flow situation, the Batchelor vortex becomes stable for $S>1.5$ and, consequently, the AI region is closed toward the high swirl values.

It is important to bear in mind that the plug-flow model does not take into consideration the necessarily finite thickness of the axisymmetric shear layer region around $r=R$. As a result, arbitrarily large wave numbers remain unstable, and

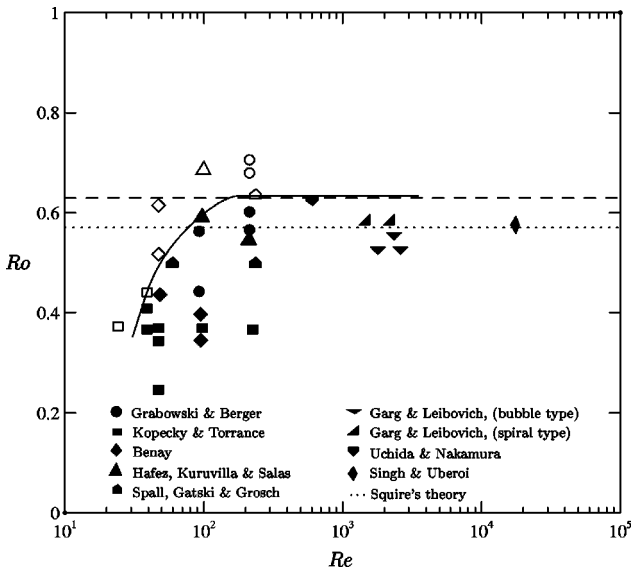

FIG. 21. Observed states in the Reynolds number–Rossby number plane for various numerical and experimental studies of swirling flows and trailing wing-tip vortices. The open symbols denote no breakdown and the solid symbols denote breakdown. After Spall, Gatski, and Grosch.[26] The dashed line (– – –) corresponds to the CI/AI transition for a Rankine vortex with plug flow and a zero external axial velocity ($a=0$).

there is no cutoff wave number, so that causality cannot strictly be enforced. However, it has been checked that the present results are robust when surface tension effects are included in order to attenuate high wave numbers and thereby ensure the causal nature of the instability.

The above analysis predicts that zero axial external flow jets ($a=0$) exhibit a transition to AI via the $m=-2$ mode as the swirl reaches $S=1.61$ (see Fig. 20). The associated critical value of the Rossby number $\mathrm{Ro}=S^{-1}=0.62$ has been represented as a dashed line in the Reynolds number–Rossby number plane of Fig. 21, together with various existing experimental and numerical results on vortex breakdown compiled by Spall, Gatski, and Grosch.[26] In spite of its simplicity, the AI/CI ''criterion'' is seen to provide a reasonable estimate of vortex breakdown onset. The AI/CI criterion ''predicts'' a transition to a predominant $m=-2$ configuration, whereas fully mature vortex breakdown is primarily associated with modes $m=0$ or $m=\pm 1$ (see, for instance, Lambourne and Bryer[27] and Sarpkaya[28]). However, swirling jet experiments by Billant *et al.*[8] indicate that the precursor state immediately preceding vortex breakdown onset prominently displays an $m=2$ symmetry, as shown in Fig. 22, a feature that is in qualitative agreement with the theoretical results for coflowing jets. In order to establish a more definite relationship between these experimental observations and the present theoretical considerations, we would have to undertake the AI/CI analysis on the effective measured velocity profiles before and after vortex breakdown onset.

ACKNOWLEDGMENTS

The authors are grateful to Ivan Delbende and Cornel Olendraru for fruitful and illuminating discussions. As always, the friendly research environment of LadHyX is warmly acknowledged. This work was financially supported by the Direction des Recherches, Etudes et Techniques of the French Ministry of Defense under Grant No. 92-098.

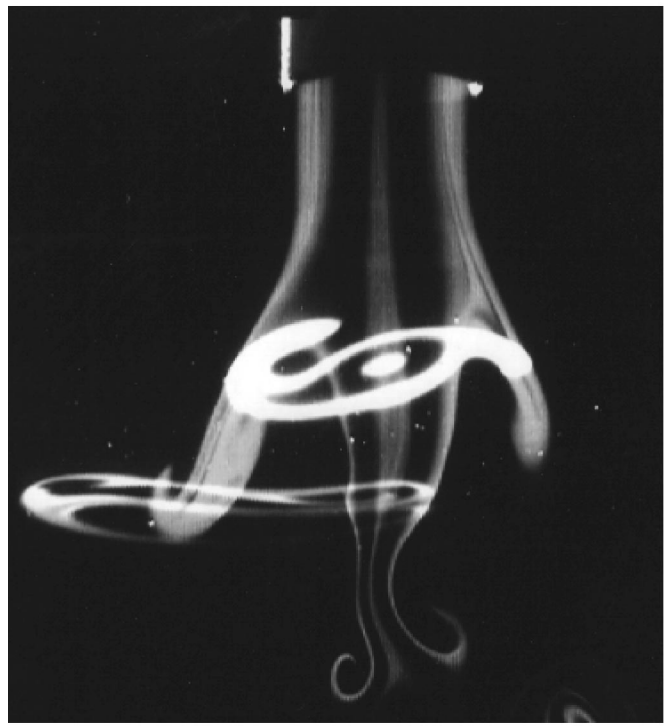

FIG. 22. Flow visualization of the precursor state in the swirling jet experiment of Billant *et al.*[8] prior to vortex breakdown onset. Overlaid vertical and horizontal laser sheets showing the double helical pattern dominated by $|m|=2$.

[1] P. Huerre and P. A. Monkewitz, ''Local and global instabilities in spatially developing flows,'' Annu. Rev. Fluid Mech. **22**, 473 (1990).
[2] R. J. Lingwood, ''Absolute instability of the boundary layer on a rotating disk,'' J. Fluid Mech. **299**, 17 (1995).
[3] G. K. Batchelor and A. E. Gill, ''Analysis of the stability of axisymmetric jets,'' J. Fluid Mech. **14**, 529 (1962).
[4] W. Thomson, ''Vibrations of a columnar vortex,'' Philos. Mag. **10**, 155 (1880).
[5] D. W. Moore and P. G. Saffman, ''The motion of a vortex filament with axial flow,'' Philos. Trans. R. Soc. London, Ser. A **A272**, 403 (1972).
[6] P. G. Saffman *Vortex Dynamics* (Cambridge University Press, Cambridge, 1992).
[7] J. Panda and D. K. McLaughlin, ''Experiments on the instabilities of a swirling jet,'' Phys. Fluids **6**, 263 (1994).
[8] P. Billant, J.-M. Chomaz, and P. Huerre, ''Experimental study of vortex breakdown in swirling jets,'' submitted to J. Fluid Mech.
[9] M. Lessen and F. Paillet, ''The stability of a trailing line vortex. Part 2. Viscous theory,'' J. Fluid Mech. **126**, 335 (1974).
[10] M. Lessen, P. J. Singh, and F. Paillet, ''The stability of a trailing line vortex. Part 1. Inviscid theory,'' J. Fluid Mech. **245**, 91 (1974).
[11] M. R. Khorrami, ''On the viscous modes of instability of a trailing line vortex,'' J. Fluid Mech. **225**, 197 (1991).
[12] C. Olendraru, A. Sellier, M. Rossi, and P. Huerre, ''Absolute/convective instability of the Batchelor vortex,'' C. R. Acad. Sci. Paris **323-IIb**, 153 (1996).
[13] I. Delbende, J.-M. Chomaz, and P. Huerre, ''Absolute/convective instabilities in the Batchelor vortex: A numerical study of the linear impulse response,'' J. Fluid Mech. (in press).
[14] H. Görtler, ''Theoretical investigations of laminar boundary layer, problem II—Decay of swirl in an axially symmetrical jet, far from the orifice,'' Air Force Contract No. AF61 (514)-627-c, 1954.

[15]M. R. Khorrami, ''Stability of a compressible axisymmetric swirling jet,'' AIAA J. **33**, 650 (1995).
[16]T. B. Benjamin, ''Theory of the vortex breakdown phenomenon,'' J. Fluid Mech. **14**, 529 (1962).
[17]C.-Y. Tsai and S. E. Widnall, ''Examination of a group-velocity criterion for breakdown of a vortex flow in a divergent duct,'' Phys. Fluids **23**, 864 (1980).
[18]R. E. Caflisch, X. Li, and M. J. Shelley, ''The collapse of an axisymmetric swirling vortex sheet,'' Nonlinearity **6**, 843 (1993).
[19]J. E. Martin and E. Meiburg, ''On the stability of the swirling jet shear layer,'' Phys. Fluids **6**, 424 (1994).
[20]M.-H. Yu and P. A. Monkewitz, ''The effect of nonuniform density on the absolute instability of two-dimensional inertial jets and wakes,'' Phys. Fluids A **2**, 1175 (1990).
[21]V. Krishnamoorthy, ''Vortex breakdown and measurements of pressure fluctuations over slender wings,'' Ph.D thesis, Southampton University, 1966.
[22]P. G. Drazin and W. H. Reid, *Hydrodynamic Stability* (Cambridge University Press, Cambridge, 1981).
[23]S. Leibovich, S. N. Brown, and Y. Patel, ''Bending waves on inviscid columnar vortices,'' J. Fluid Mech. **173**, 595 (1986).
[24]The absolute frequency ω_0 should not be confused with the various axisymmetric temporal modes $\check{\omega}_0^{\pm}$, $\omega_{0,n}$, ω_0^{kh} considered in Sec. III.
[25]Positive helical modes may also undergo a transition to AI, but the corresponding transition curves are always located within the shaded region of Fig. 20: they are never critical.
[26]R. E. Spall, T. B. Gatski, and C. E. Grosch, ''A criterion for vortex breakdown,'' Phys. Fluids **30**, 3434 (1987).
[27]N. C. Lambourne and D. W. Bryer, ''The bursting of leading-edge vortices: Some observations and discussion of the phenomenon,'' Aeronautical Research Council, Report & Memoranda R. & M., 1961, Vol. 3282, p. 1.
[28]T. Sarpkaya, ''On stationary and travelling vortex breakdowns,'' J. Fluid Mech. **45**, 545 (1971).